Research Article

Experimental Study of Multiple Physical Parameters Monitoring during Uniaxial Loading Process of Sandstone

Yongchuan Zhao [ID],[1,2] Tianhong Yang [ID],[2] and Wenhao Shi [ID][2,3]

[1]*College of Civil Engineering and Architecture, Hebei University, Baoding 071002, China*
[2]*School of Resources and Civil Engineering, Northeastern University, Shenyang 110819, China*
[3]*School of Civil Engineering, Suzhou University of Science and Technology, Suzhou 215011, China*

Correspondence should be addressed to Yongchuan Zhao; yongchuanzhao@sina.com and
Tianhong Yang; yangtianhong@mail.neu.edu.cn

Aiming at the damage evolution and energy release characteristics of sandstone in failure process, uniaxial and cyclic loading experiments were conducted with the average temperature, infrared temperature field, acoustic emission (AE), and displacement field being monitored simultaneously. The results show that in the low stress stage, the initial pores and fissures are compressed and the thermoelastic effect is insignificant. At the same time, the AE events are active, but most of the events are released with low energy. Then, the surface of the specimen shows stratified displacement phenomenon in the vertical direction. In the following stage, the thermoelastic effect is significant, and the average temperature of specimens shows a linear correlation with stress, whereas the AE is relatively inactive, and vertical surface deformation shows further homogenization and saliency. Because of the top and bottom constraints, the horizontal displacement field shows axis symmetrical distribution of double half-ellipse like a drum. During the yielding phase and the rupture moment, the average temperature rises obviously because of the heat from the friction of the rupture surface, and the temperature field also appears the phenomenon of differentiation; in the meantime, a large amount of AE events occur and the proportion of high energy events increases; further, the deformation field is significantly gathered near the ruptured position. Finally, the time sequence of the multiple physical parameters (AE parameters, average temperature, temperature fields, horizontal and vertical displacement fields) is summarized, which can be a reference for the stress state and failure analysis.

1. Introduction

The failure of rock is the result of interior crack initiation, propagation, and penetration. The whole rupture process of rock is a complex physical phenomenon. With the increasing load, many physical parameters, including the force, deformation, elastic wave [1], thermal energy [2, 3], electric potential [4], and resistivity [5], will occur abnormal variations. These abnormal signals are very important for predicting the instability and quantifying the damage degree.

The energy evolution plays an important role in explaining the mechanism of rock engineering disasters. The energy input by the loading machine can transform and release in multiple forms, such as elastic deformation, plastic deformation [6], infrared heat radiation, elastic wave, and electric energy. The initiation and expansion of microcracks will cause energy

release in the form of acoustic emission (AE), which has been used for the prediction of quantitative rock damage widely [7]. The friction caused by microcrack and the thermoelastic effect will increase infrared temperature [8]. Further, the relationship between the infrared radiation temperature and stress has been discussed by bending and shearing experiments [9]; the experiment makes it possible to measure the stress level by the noncontact method. On the other hand, the specimens deformation (elastic and plastic deformation) is also a result of energy transformation, and the digital image correlation (DIC) technology can be used to monitor and inverse the full-field deformation [10]. With the characteristic of high frequency and noncontact, the DIC technology is usually used in the complicated and harsh circumstances, such as in high temperature [11] or polluted environment. Compared with the traditional measure method such as using extensometer or

strain gauge, the full-field monitoring of DIC has a great advantage in obtaining the full-field deformation rather than the strain at a point [12, 13].

From the above studies, it is clear that the variation characteristics of infrared radiation temperature, full-field deformation, and AE are quite meaningful for quantifying damage and explaining the failure mechanism [14, 15], and the monitoring of single physical quantity has been widely researched. But the joint monitoring of multiple physical quantities is more comprehensive for understanding and analyzing the internal damage evolution process. By now, some joint monitoring systems have been established, such as the multiparameter comprehensive monitoring system (including microseismic, charge induction, AE, microcomputed tomography, and scanning electron microscopy) [16, 17–19]. The joint monitoring systems show that comprehensive use of multimethod monitoring is a potential method for analyzing the rock failure process in multiple views.

Thus, in this paper, the uniaxial and cyclic loading of sandstone specimens have been conducted. During the loading process, the average temperature, infrared radiation temperature field, AE activity, vertical displacement fields, and horizontal displacement fields have been monitored simultaneously. Based on the obtained multiple physical parameters, the chronological order of multi-physics parameters has been analyzed, and the chronological order can be a guidance for the failure warning and damage quantifying.

2. Specimens Preparation and Loading Schemes

The mesozoic sandstone drilled from Xiaojihan coal mine, located in the city of Yulin, China, was prepared for the experiments. All the specimens were cut into standard cylinder shape with 50 mm diameter and 100 mm length in accordance with the ISRM. The tests were carried out on the TYJ-500 kN loading machine with a loading speed of 0.001 mm/s in the axial direction.

During the experiments, the average temperature was measured by Fluke 568 Thermometer with wavelength of 8–14 μm. Infrared temperature field was collected by H2640 imager with wavelength of 8–13 μm. The AE monitoring was conducted by PAC PCI-II AE system, which includes a Nano30 piezoelectric sensor with response frequency of 125–750 kHz, and the sensor was arranged in the middle area of the cylindrical specimen. The images used for the DIC were obtained by XTDIC speckle system with 2.3 million pixels. The related testing equipment is shown in Figures 1 and 2.

In the experiment, 12 sandstone specimens were prepared for the experiment, the loading paths contained uniaxial loading and cyclic loading, in the uniaxial loading experiments, the specimens were compressed to failure directly, and in the cyclic loading process, the maximum pressure of each cyclic loading increased 10 kN until the failure. The loading paths and monitoring methods are shown in Table 1.

In the experiment, the energy of average temperature and infrared image correspond to thermal energy, AE energy
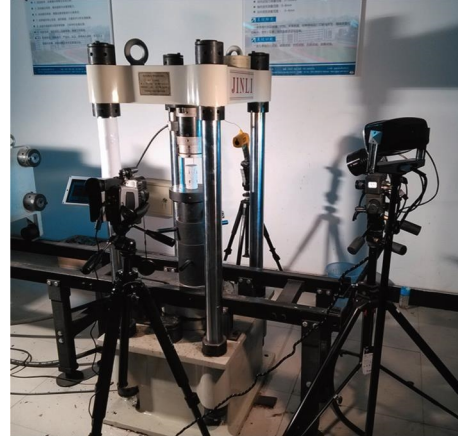

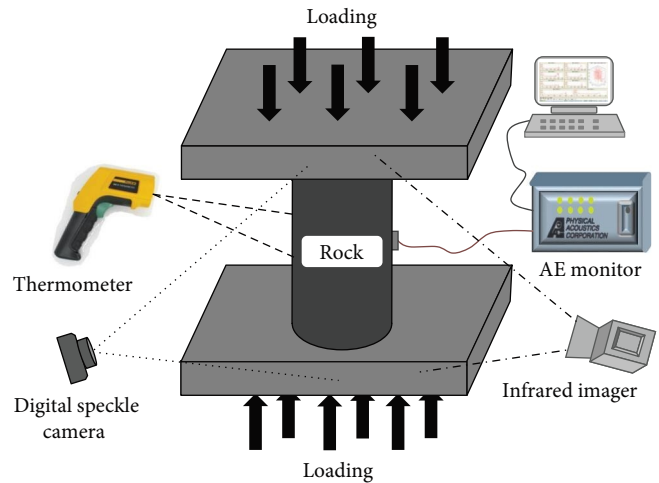FIGURE 1: The loading and monitoring system.

FIGURE 2: Diagrammatic sketch of loading and monitoring system.

corresponds to elastic wave energy (from a microfracture inside the rock), and displacement field of DIC corresponds to elastic and plastic deformation energy; all the energy come from the energy input by the press machine during the loading process.

3. The Variations of Multiple Physical Parameters during the Loading Process

3.1. The Average Temperature Variation Laws during Loading Process. Some theories and experiments have concluded that the solid material shows thermoelastic and thermoplastic effect during the loading process. Compared with thermoplastic, the study of thermoelastic theory is more systemic and deeply [20]. In a system considering heat transmitting, the relationship between temperature and elastic deformation is shown in Equation (1) [21]:

$$\Delta T = \frac{T}{\rho C_\varepsilon} \sum_{i,j=1,2,3} \frac{\partial \sigma_{ij}}{\partial T} \varepsilon_{ij} + \frac{Q}{\rho C_\varepsilon}, \tag{1}$$

TABLE 1: Loading paths and monitoring methods.

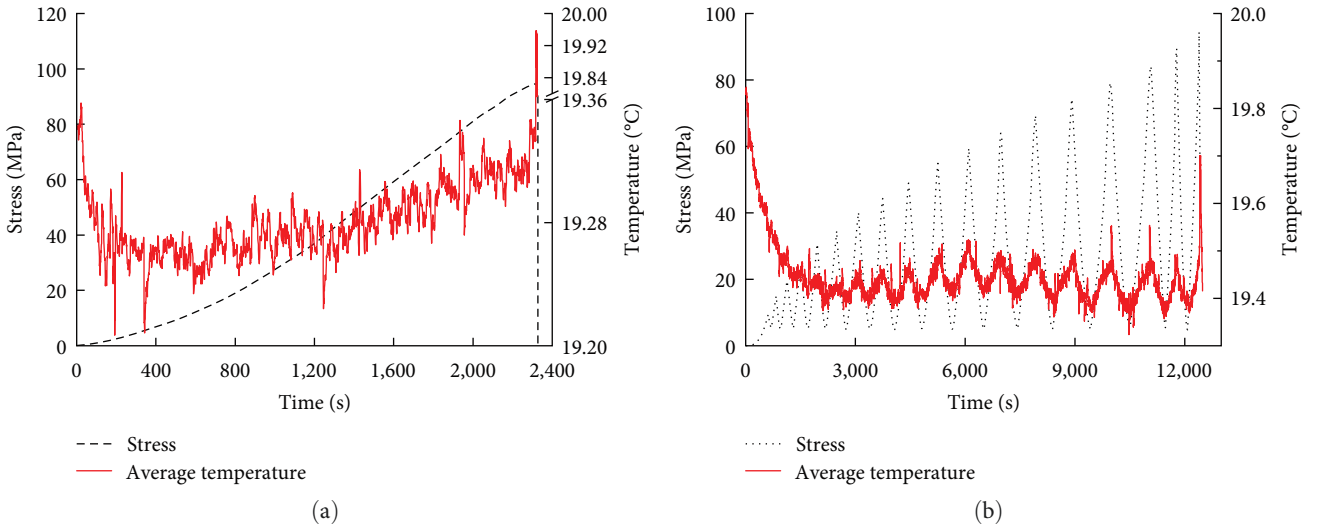| Loading paths	Specimens	Average temperature	AE	DIC image	Infrared temperature image
Cyclic loading	A2Q	√	√		
	D9	√	√		
	D10Q	√	√		
	H16	√	√		
	H17	√	√		
	H18	√	√		
Uniaxial loading	A10Q	√		√	
	A16Q	√	√	√	√
	H19	√	√	√	√
	H20	√	√	√	√
	H21	√	√	√	√
	H22	√		√	√

(a)

(b)

FIGURE 3: The average temperature variation in the loading process. (a) The specimens of H21. (b) The specimens of H16.

where T is the absolute temperature, C_ε is the specific heat capacity of the material at constant strain, Q is the heat input or output, ρ is the mass density, σ_{ij} is the stress change tensor, and ε_{ij} is the strain change tensor.

For isotropic elastic material, the Equation (1) is simplified to:

$$\Delta T = -\frac{\alpha}{\rho C_p} T \sum_{i,j=1,2,3} \sigma_{ii} + \frac{Q}{\rho C_\varepsilon}, \tag{2}$$

where α is the coefficient of linear thermal expansion, C_p is the specific heat capacity at constant pressure, and $\sum \sigma_{ij}$ is the first stress invariant.

Aimed at the thermal phenomenon in the loading process, massive studies have been developed in the uniaxial loading test [5, 22]. However, because of the limit of the sampling frequency, few experiments are conducted to obtain the temperature data directly by a thermometer. Based on the high-frequency and high-precision temperature

acquisition instrument, the average temperature of sandstone with different loading paths has been investigated.

As shown in Table 1, six specimens were conducted for the uniaxial loading experiment. In the average temperature experiment, there are four specimens showing declining trend at low stress stage, then during the elastic and plastic stage, the average temperature increases stably, and finally reaches highest temperature at the failure moment. The typical temperature variation trend is shown in Figure 3(a). However, there are two specimens showing declining trend during the whole loading process, and only an abrupt increase occurs at the failure moment.

For the cyclic loading experiments, also six specimens were conducted, as shown in Table 1. All the specimens show the same variation trend. At low stress level, the average temperature shows declining trend, and in the following cyclic loading, the average temperature shows notable linear positive correlation with the stress, namely, the thermoelastic effect is remarkable. Moreover, the temperature shows serious increasing trend at the failure moment, and the typical average temperature variation is shown in Figure 3(b).
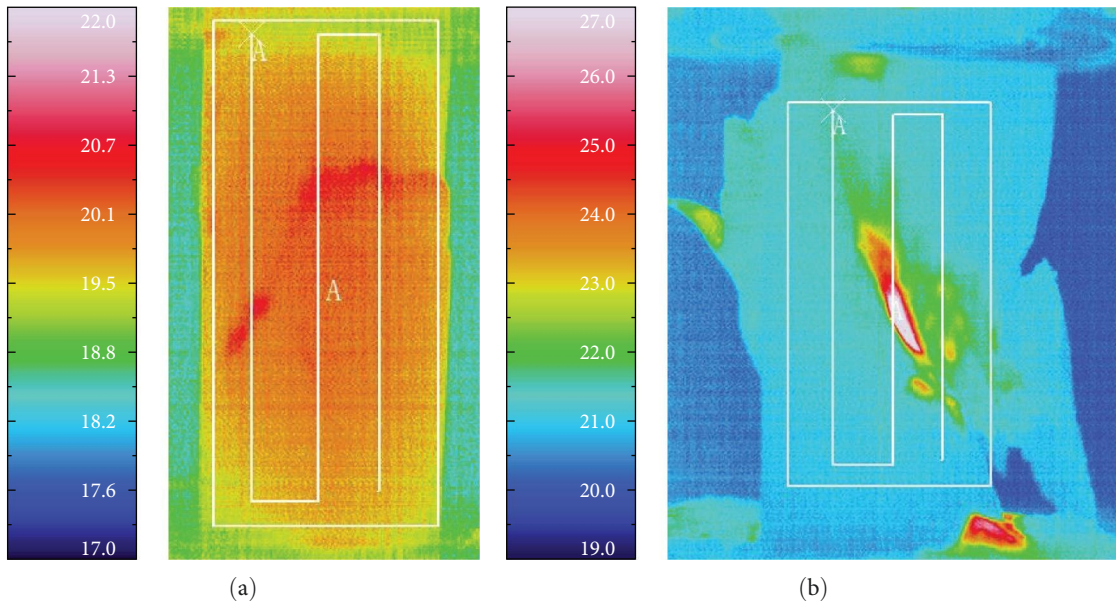
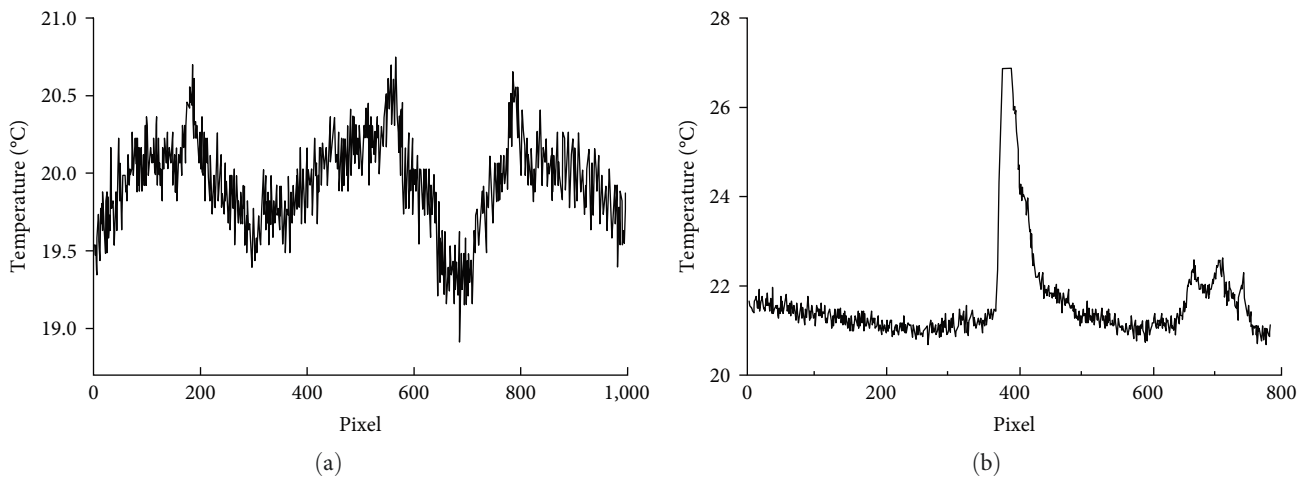FIGURE 4: The infrared images at the failure moment. (a) Infrared image of A16Q. (b) Infrared image of H21.

FIGURE 5: The temperature variation on the measuring line at the failure moment. (a) Temperature variation of A16Q. (b) Temperature variation of H21.

The reason of average temperature dropping at the initial loading stage is that the fracture and cracks in the specimens are closed in the initial stage, and the specimens mainly show plastic deformation, so the thermoelastic effect is not remarkable. Moreover, the steel machine starts contacting with the specimens closely, and the steel is a better heat conduct material resulting in the heat of the specimens transferring to the machine, so the temperature of specimens decreases. After a period of contacting, the heat transferring between rock and machine reaches a balance, and also the specimens enter elastic stage, so the primary stress and the primary strain show linear relationship, and because of thermoelastic effect, the average temperature variation is consistent with the stress increasing and declining. At last, when the specimen reaches its peak strength, the deformation converges in the failure zone, and the friction effect of particles is

also serious; meanwhile, the elastic wave may cause particles vibration at a high frequency; all the above factors may cause the temperature increasing, so the average temperature increases sharply at the failure moment.

3.2. The Infrared Radiation Characteristic of Temperature Field. The thermometer has the characteristic of high frequency and high sensitivity, but the temperature obtained is the average value in a small zone, and it can not reflect the temperature field variation. With the purpose of analyzing the temperature field, the infrared radiation images have been collected in the test simultaneously.

In the previous study, it is concluded that the infrared image shows alienation phenomenon and the average infrared radiation temperature (AIRT) shows abnormal trend. Some studies show that the failure pattern may also affect

the temperature, the shearing fracture may cause the temperature increase, and the splitting fracture may cause the temperature decline [3, 23].

In this part, the H2640 infrared radiation imager was used to monitor the temperature field of the specimens surface. Due to the effect of the environment variation (including the light and human body radiation), during the test, the windows and curtains were closed, and the unnecessary activities were forbidden.

The typical results are shown in Figure 4; it can be found that the temperature is not evenly distributed on the specimens surface. When the rock reaches its peak strength, the infrared images show differentiation characteristic, the temperature of nonfailure zone keeps stable, and that of failure zone releases massive heat because of shearing crack and the friction of particles; the released energy leads to a seriously increase in the temperature.

Further, with the purpose of studying the temperature variation in different zones, a measuring line (white line) is located on each picture, as shown in Figure 4, and the temperature value on the measuring line has been extracted. The temperature of the measuring line with the length of the measuring line (pixel points) is shown in Figure 5. It is clear that the temperature increases seriously in the failure zone, and the highest temperature (as shown in Figures 5(a) and 5(b)) of typical specimens of A16Q and H21 increases to 1 and 5°C, respectively, which is similar with the previous research [24]. In the infrared image, it can be found that the energy produced by the shearing crack and friction is much more than the thermoelastic effect.

The variations of average temperature and infrared images show that in the initial loading stage, the specimens show more plastic deformation, and the thermoelastic effect is not obvious; due to the heat transforming between the rock and machine, the average temperature shows declining trend. In the elastic stage, thermoelastic effect is notable, and the temperature shows linear relationship with the stress. At the failure moment, massive heat is produced in the failure zone because of shearing cracks and friction, and the infrared image shows differentiation phenomenon, the average temperature increases sharply.

3.3. Characteristic of Acoustic Emission Parameters in the Loading Process.

In the rock failure process, the radiation energy contains the thermo energy, which is expressed in the temperature increasing and elastic wave energy, which release in the form of AE. AE is the energy released by cracks initiation and propagation, and it is widely discussed in the field of crack location [25, 26], damage evaluation [27], and energy release [28] The elastic wave parameters include amplitude, energy, ring counts, rising time, and frequency; these parameters are meaningful for the damage analysis [29], and also these AE parameters can be calculated from the AE waveform. The part-related parameters are shown in Figure 6.

In AE studies, the ringing counts, energy, and b value based on the AE wave are chosen for studying the energy release and damage evolution. The b value is a universal
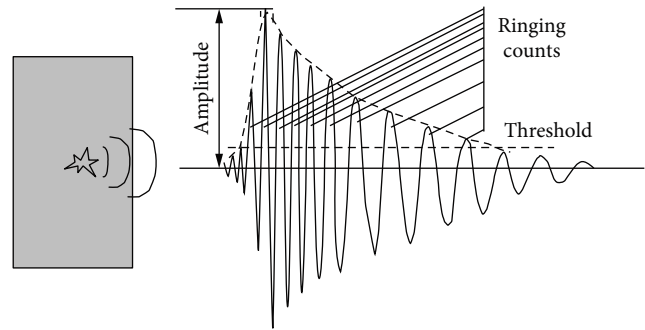

FIGURE 6: Diagram of acoustic emission parameters.

parameter in the earthquake domain; it means that the earthquake frequency declines in the exponential form with the earthquake magnitude [30], and the b value decreases to a minimum at the time of failure [31]. There are many similarities between the earthquake and AE event except the magnitude and frequency, and so many methods and theory of earthquake are cited in the AE studies. In the AE monitoring system, the Nano30 sensor receives the voltage signal and transmits the signal into the acquisition card. So, compared with the earthquake signal, the AE number and the amplitude obey the following equation [32] as follows:

$$\lg(N) = a - b \times (A\mathrm{dB}/20), \qquad (3)$$

where A_{dB} is the signal maximum amplitude, N is number of events larger than magnitude A_{dB}, and a and b are fitting parameters.

The fitting parameters present the proportion of the high amplitude events in the all the events. A higher b value will be obtained if most events are small events with less energy, indicating less cracks or cracks growing slowly, whereas a lower b value represents most AE events that are large events with high energy, indicating many cracks or cracks growing fast. A undulate b value meaning unstable cracks expand [6, 33], so the b value is related with the damage degree closely.

In the loading process, the typical temporal variation of b value and AE energy is shown in Figure 7. It shows that in the compaction stage, the initial pore and cracks are closed, and massive AE events occur; however, the b value is also at a high level; it means that most of the AE events produced in the initial stage are low energy. During the elastic stage, the AE events are relatively inactive, and the b value shows stable value with little variation. However, in the yield stage, the AE energy increases seriously; it means that the inner damage evolves violently; meanwhile, the b value vibrates acutely meaning that the AE events with high and low energy occur alternately. At the failure moment, the AE energy reaches its maximum, and the maximum energy value is often hundredfolds of previous value (a break is located at the counts axial, as shown in Figure 7). Further, the b value declines clearly; it means that cracks with higher energy appear in the rock, and then the failure comes. It can be seen that the AE parameters
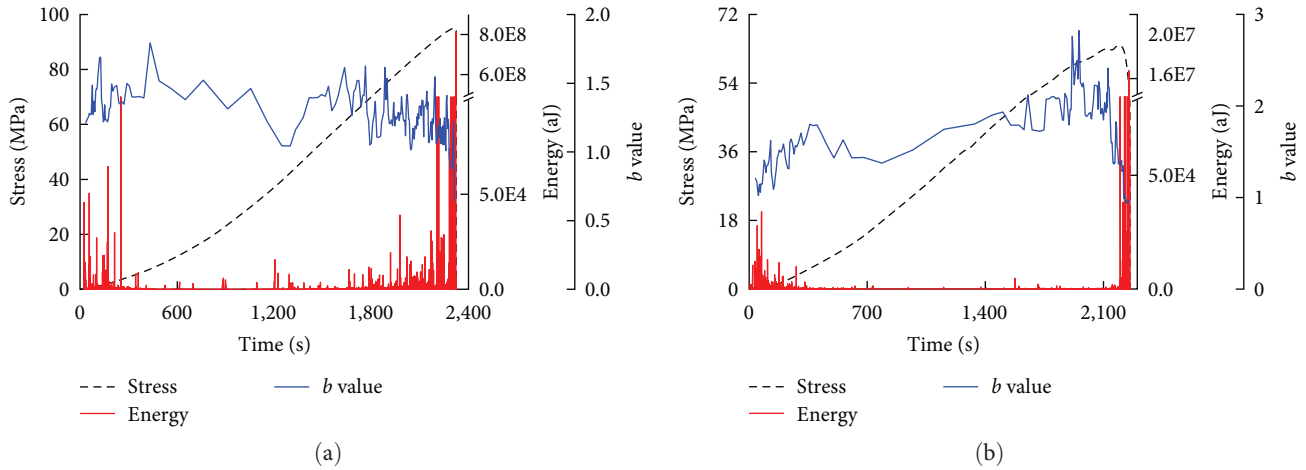
(a)

(b)

FIGURE 7: The AE characteristic during the loading process. (a) The AE characteristic of H21. (b) The AE characteristic of A16Q.
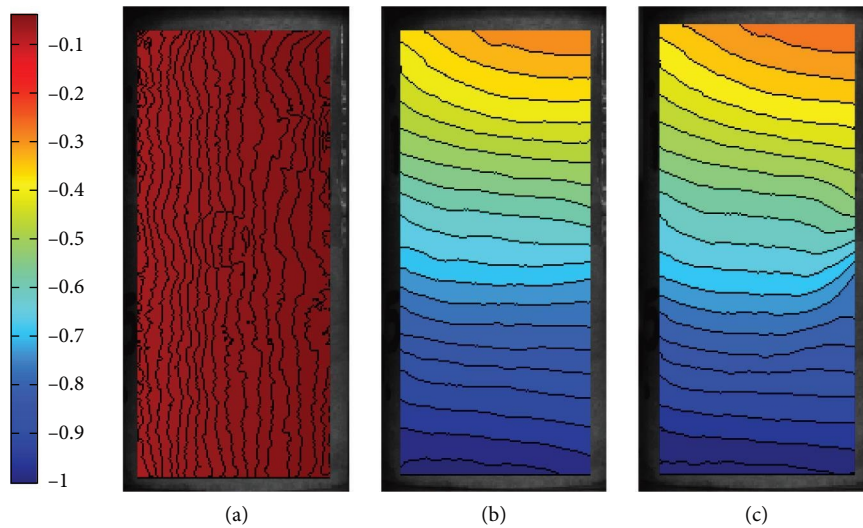

(a)   (b)   (c)

FIGURE 8: The vertical displacement fields of A16Q at different stress level. (a) Stress level = 1.6% σ_s. (b) Stress level = 96.4% σ_s. (c) Stress level = 100% σ_s.

(AE energy and b value) show different variations in different stress stage, which can be used to provide early warning for fracture instability.

3.4. Deformation Field Characteristic with the Method of Digital Image Correlation. Part of the work done by the press machine is used for radiation in the form of thermo and elastic wave, and the rest of the work is used for changing the shape of the specimens. The deformation contains elastic and plastic deformation. In the traditional deformation monitoring experiment, the deformation is usually measured by extensometer or strain gauge, which is a quite small zone deformation with the probability of losing whole deformation characteristic. In this part, a high-function digital camera and image correlation technology are used to study the displacement field characteristic in the loading process.

DIC is a new optical method, which captures images of the rock surface and obtains full-field deformation by comparing the current images with the reference image. Here, the Ncorr code is used for the DIC, Ncorr is an open-source 2D DIC program compiled by Matlab and C++ language. With the purpose of subset displacement tracking, an improved DIC based on the conventional Newton–Raphson algorithm is compiled in the code [34]. By processing the displacement field with the method of differentiation, the Green–Lagrangian strain field can be obtained [11, 35]. The image processing mainly contains setting reference image, defining deformation image and target zone, arranging reference seeds, and calculating the displacement and deformation field. Further, the code flow can map the physical dimension with the pixels, so the displacement size in the object zone is the real deformation scale. Some studies show that the deformation result of Ncorr is consistent with the commercial 2D DIC packages [36]; it means the deformation processed by the Ncorr is reliable and reasonable.

Figure 8 shows the vertical displacement variation at different stress level. According to the loading machine principle, in the axial loading process, the upper platen is fixed, and the lower platen moves toward to the upper one as the
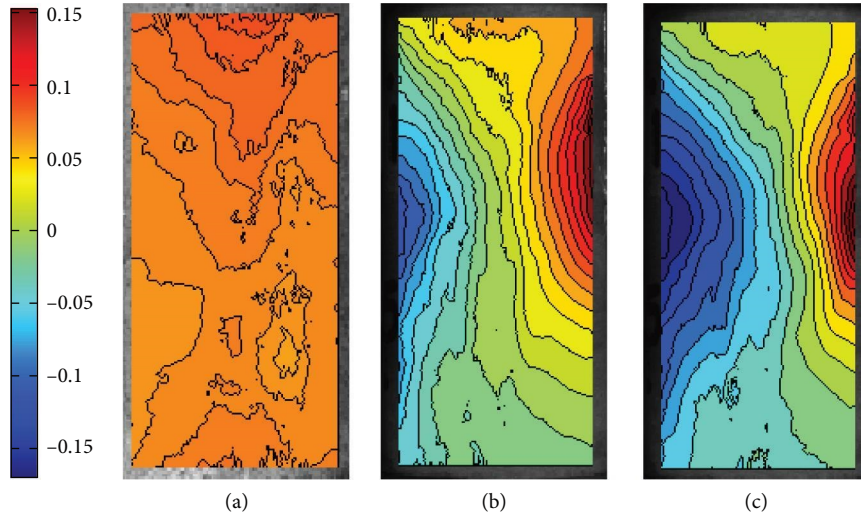
FIGURE 9: The horizontal displacement fields of A16Q at different stress level. (a) Stress level = 1.6% σ_s. (b) Stress level = 96.4% σ_s. (c) Stress level = 100% σ_s.
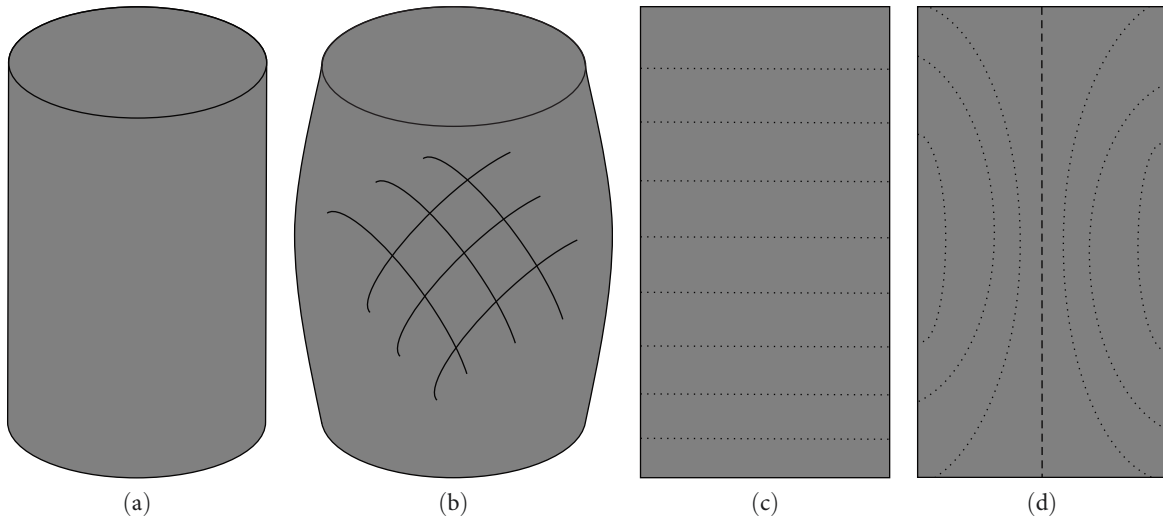

FIGURE 10: Schematic diagrams of displacement field. (a) Initial state. (b) Drum expanding. (c) Vertical displacement. (d) Horizontal displacement.

setting rate (0.001 mm/s). It can be found that at low stress level (Figure 8(a)), the vertical displacement field shows disordered pattern. With the increasing stress, the displacement field shows evenly stratified characteristic. The lower and upper faces have the biggest and smallest displacement, respectively (Figure 8(b)). When the stress reaches the peak strength, the displacement image shows the concentration and heterogeneity, and the zone with concentrated displacement contour is also the failure zone in the next step.

In the uniaxial loading process, there is no limit in the radial direction around the specimens, so the expansion effect exists. Figure 9 shows the horizontal displacement characteristic. In the low stress level (Figure 9(a)), the displacement shows no regular pattern, similar with vertical displacement. As the stress increases (Figure 9(b)), the horizontal displacement shows particular characteristic. In the axial line, the horizontal displacement is quite small, and the zone far

from the axial line shows obvious expanding trend. Moreover, because of the friction between the loading platen and specimens, the expanding of the top and bottom of specimens is limited, so the displacement in the horizontal direction is much smaller than that of other zone; thus, the middle of the specimen shows biggest displacement. The whole horizontal displacement field shows axis symmetrical distribution as double half-ellipse. In the failure moment, the horizontal displacement also shows heterogeneity characteristic clearly.

In above DIC analysis, it can be summarized that the length of specimens in the axial direction is evenly compressed, as shown in Figure 10(c), and the radial size shows the phenomenon of expanding, but there is a friction force between indenter of the machine and the top (bottom) end faces of the specimen, which restricts the radial expansion of the two end faces, so the middle part bulges freely and end faces (top and bottom) restrict bulging, as shown in Figure 10(d). The displacement in vertical
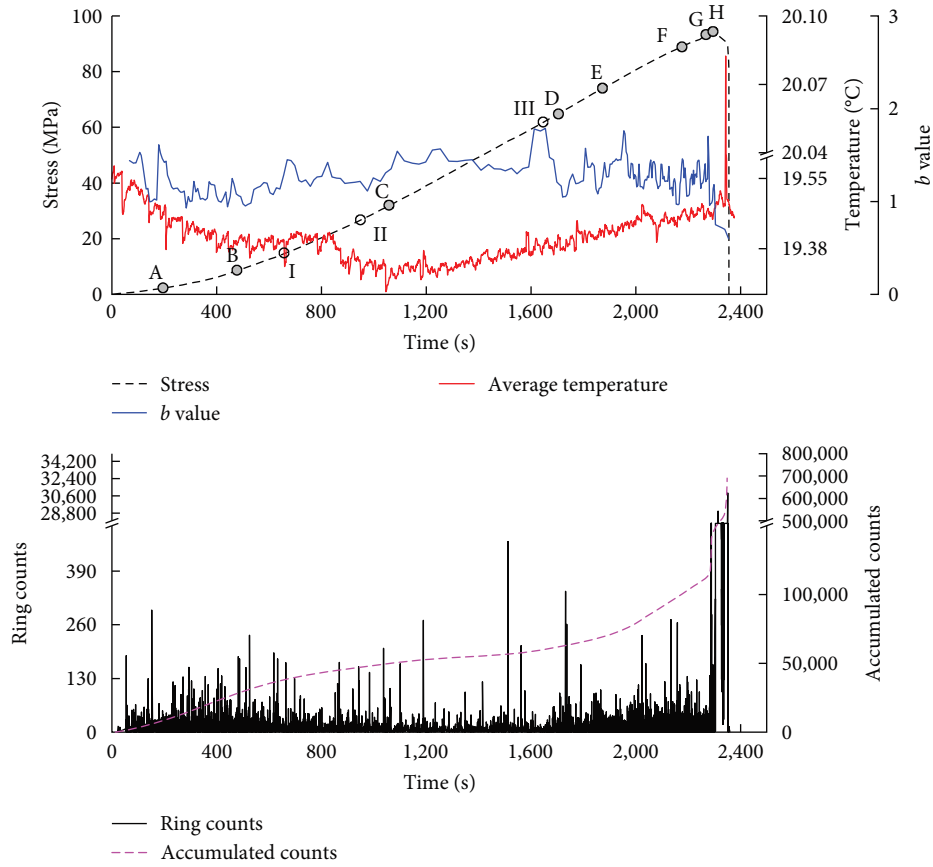
(a)
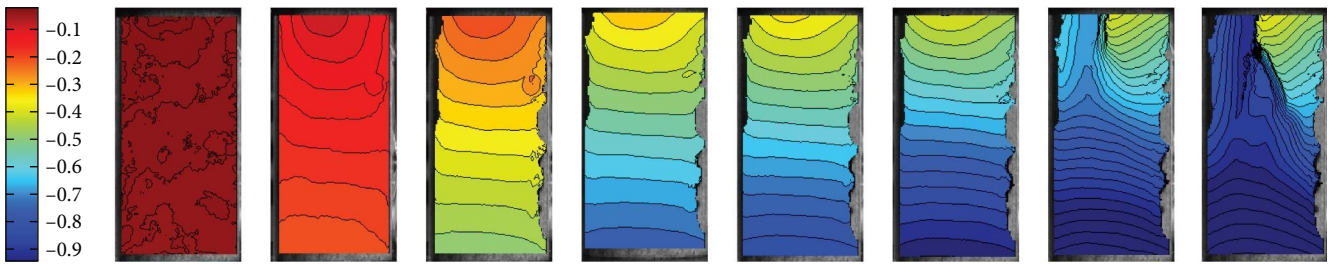
(b)
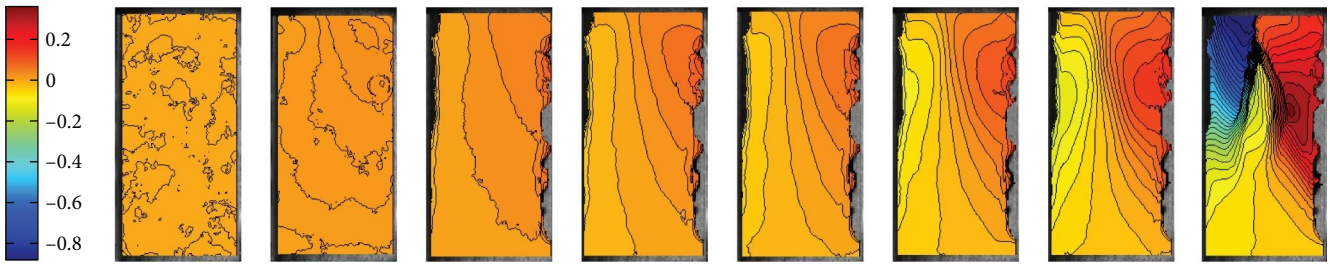
(c)

Figure 11: The multiple physical parameters variation of H20. (a) The variation of AE and temperature characteristic of H20. (b) Typical vertical displacement fields of H20. (c) Typical horizontal displacement fields of H20.

Stress level (%)	0	20	40	60	80	100

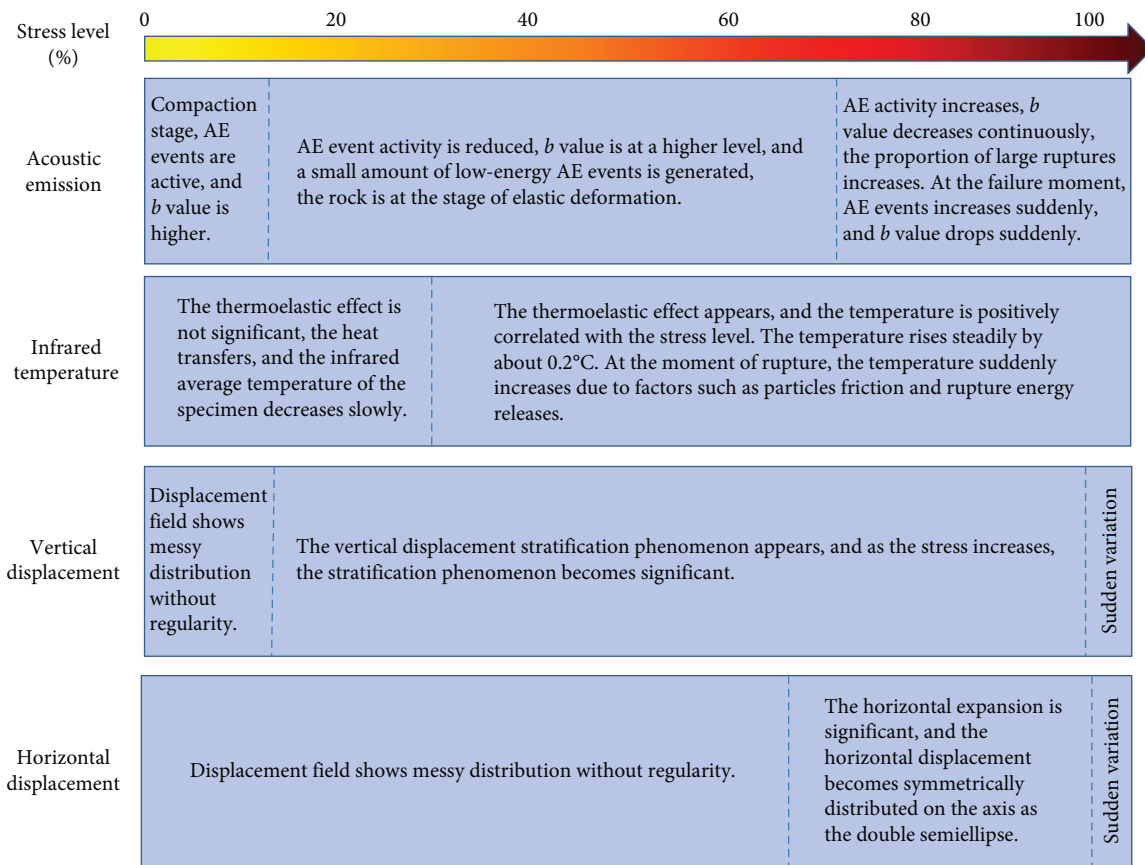|					
Acoustic emission	Compaction stage, AE events are active, and b value is higher.	AE event activity is reduced, b value is at a higher level, and a small amount of low-energy AE events is generated, the rock is at the stage of elastic deformation.		AE activity increases, b value decreases continuously, the proportion of large ruptures increases. At the failure moment, AE events increases suddenly, and b value drops suddenly.	
Infrared temperature	The thermoelastic effect is not significant, the heat transfers, and the infrared average temperature of the specimen decreases slowly.	The thermoelastic effect appears, and the temperature is positively correlated with the stress level. The temperature rises steadily by about 0.2°C. At the moment of rupture, the temperature suddenly increases due to factors such as particles friction and rupture energy releases.			
Vertical displacement	Displacement field shows messy distribution without regularity.	The vertical displacement stratification phenomenon appears, and as the stress increases, the stratification phenomenon becomes significant.			Sudden variation
Horizontal displacement	Displacement field shows messy distribution without regularity.			The horizontal expansion is significant, and the horizontal displacement becomes symmetrically distributed on the axis as the double semiellipse.	Sudden variation

FIGURE 12: The time sequence characteristic of multiple physical parameters variation during the loading process.

direction shows uniformly-layered characteristic and the displacement in horizontal direction shows axis symmetrical distribution as double half-ellipse. So, the cylindrical specimens exhibit deformation of drum shaped, as shown in Figure 10(b).

4. The Time Sequence Characteristics of Multiple Physical Parameters Variation in the Process of Rock Failure

It can be seen from the above analysis that the characteristic, including surface temperature field, AE activity, and surface displacement field of the specimen, shows significant regular variation during the loading process. Further, the change characteristics and sequence of different physical quantities have certain guiding significance for explaining the damage mechanism.

Taking the H20 as an example, the stress curve, the surface average temperature curve, and the AE characteristic curves are integrated, as shown in Figure 11(a), and three marked points (I, II, III) are arranged on the stress curve. It can be seen that the AE ring counts increase rapidly with a high b value before marked point I (stress level 15.8%), so the AE energy value is relatively low. It means that the initial fissures inside the rock are compacted. Between marked points I and III (stress level 65.84%), the AE ringing counts increase slowly, and the b value is still at a high level, indicating that a small amount of low energy AE events is

generated in the rock, and the rock is at elastic deformation stage. After marked point III, the AE ring counts increase continuously, and the b value continues to decrease; it means that the high energy ruptures in the rock occur. At the moment of the rupture, the AE events suddenly increase, and the b value suddenly decreases. Before marked point II (stress level 28.5%), the thermoelastic effect in the compaction stage is not significant, and the specimen releases heat to the outside, causing the average temperature to decrease continuously. After marked point II, the average temperature begins to rise steadily, it shows a positive correlation with the stress level, and the average temperature increases about 0.2°C before the peak strength. At the moment of failure, the average temperature increases sharply due to the sliding friction of the mineral particles and the release of fracture energy.

Moreover, the representative pictures of the displacement fields in the vertical and horizontal directions of H20 are shown in Figures 11(b) and 11(c), and the serial numbers are correspond with the marked points (A. B. C… H) on the stress curve, as shown in Figure 11(a); it can be seen that at point A (stress level 2.13%), both the vertical and horizontal displacement fields appear irregular and random characteristic. At point B (stress level 9.04%), the vertical displacement field begins to be stratified, and the horizontal displacement field is still irregular. Then, as the stress increases, the stratification of vertical displacement field becomes more obvious.

Until point D (stress level 70.21%), the horizontal displacement field begins to appear axisymmetric semielliptical characteristics, which means that the specimen begins to appear regular expansion in the radial direction. With the further increase of the stress, at point G (stress level 99.14%) and H (stress level 99.78%), the vertical and horizontal displacement fields begin to show the characteristics of deformation accumulation, respectively, which mean that the rock is about to appear instability.

The AE, infrared temperature field, average temperature, and vertical and horizontal displacement fields of all specimens in the uniaxial loading experiment are processed as the above method. To avoid errors and contingencies, the stress levels of each physical quantity changing characteristic points are averaged. The comprehensive analysis of the time sequence characteristics of multiple physical parameters during the loading process is shown in Figure 12. As shown in Figure 12, the time sequence and variation laws of AE, infrared temperature, vertical displacement, and horizontal displacement with the stress level are clearly presented; the sequence and the sensitivity of physical quantities can be an effective reference for analyzing the rock failure mechanism and determining the degree of damage.

5. Conclusion

In the uniaxial and cyclic experiments, the multiple physical parameters, including AE, infrared temperature field, average temperature, and vertical and horizontal displacement field, have been monitored simultaneously, and the variation and the time sequence of physical parameters have been obtained. The following conclusions can be drawn:

(1) In the initial loading stage, the AE events are active, but most of the AE events are released with low energy. In the elastic stage, the AE events are not active, and the energy of most AE events is lower. In the high stress level, the AE events increase rapidly, and the b value declines constantly, which mean the proportion of higher AE energy is increasing and the failure moment is coming.

(2) In the initial loading stage, the temperature shows declining trend due to the specimens releasing energy to the outside. In the elastic stage, the specimens show obvious thermoelastic effect, and the temperature and the stress show linear relationship. At the failure moment, the temperature increases suddenly, and, further, the infrared images show differentiation and concentration phenomenon; the temperature in failure zone increases clearly because of particles friction and cracks propagation.

(3) In the initial loading stage, the vertical and horizontal displacement fields both appear irregular and random phenomenon. In the elastic stage, the vertical displacement shows stratified evenly characteristic, and at high stress level, the horizontal displacement shows axis symmetrical distribution as double half-ellipse.

Near the failure moment, the displacement fields both show clearly inhomogeneous characteristic.

(4) The multiple physical parameters of all specimens are comprehensively analyzed, and the time sequence characteristics of AE activity, average temperature, temperature field, and digital displacement fields (horizontal and vertical direction) are obtained. This multiple physical sequence feature can be used for analyzing rock failure mechanism and early warning of rock instability.

Data Availability

The data used to support the findings of this study are available from the corresponding author upon request.

Conflicts of Interest

The authors declare that they have no conflicts of interest.

Acknowledgments

References

[1] P. Zhang, T. Yang, Q. Yu et al., "Microseismicity induced by fault activation during the fracture process of a crown pillar," *Rock Mechanics and Rock Engineering*, vol. 48, no. 4, pp. 1673–1682, 2015.

[2] R. Steinberger, T. I. V. Leitão, E. Ladstätter, G. Pinter, W. Billinger, and R. W. Lang, "Infrared thermographic techniques for non-destructive damage characterization of carbon fibre reinforced polymers during tensile fatigue testing," *International Journal of Fatigue*, vol. 28, no. 10, pp. 1340–1347, 2006.

[3] L. Wu, C. Cui, N. Geng, and J. Wang, "Remote sensing rock mechanics (RSRM) and associated experimental studies," *International Journal of Rock Mechanics and Mining Sciences*, vol. 37, no. 6, pp. 879–888, 2000.

[4] Z. Li, X. Zhang, Y. Wei, and M. Ali, "Experimental study of electric potential response characteristics of different lithological samples subject to uniaxial loading," *Rock Mechanics and Rock Engineering*, vol. 54, no. 1, pp. 397–408, 2021.

[5] Z.-H. Li, Q. Lou, E.-Y. Wang, S.-J. Liu, and Y. Niu, "Study on acoustic–electric–heat effect of coal and rock failure processes under uniaxial compression," *Journal of Geophysics and Engineering*, vol. 15, no. 1, pp. 71–80, 2018.

[6] Q. Liu, R. Zhang, M. Gao, G. Li, Z. Zhang, and Z. Zhao, "Acoustic emission characteristic and comprehensive failure precursors of coal under unloading condition," *Journal of Sichuan University(Engineering Science Edition)*, vol. 48, no. S2, pp. 67–74, 2016.

[7] H.-L. Lee, J.-S. Kim, C.-H. Hong, and D.-K. Cho, "Ensemble learning approach for the prediction of quantitative rock

damage using various acoustic emission parameters," *Applied Sciences*, vol. 11, no. 9, Article ID 4008, 2021.

[8] L. Wu, S. Liu, Y. Wu, and H. Wu, "Changes in infrared radiation with rock deformation," *International Journal of Rock Mechanics and Mining Sciences*, vol. 39, no. 6, pp. 825–831, 2002.

[9] P. Stanley and W. K. Chan, "Quantitative stress analysis by means of the thermoelastic effect," *The Journal of Strain Analysis for Engineering Design*, vol. 20, no. 3, pp. 129–137, 1985.

[10] A. Modiriasari, A. Bobet, and L. J. Pyrak-Nolte, "Active seismic monitoring of crack initiation, propagation, and coalescence in rock," *Rock Mechanics and Rock Engineering*, vol. 50, no. 9, pp. 2311–2325, 2017.

[11] J. Blaber, B. S. Adair, and A. Antoniou, "A methodology for high resolution digital image correlation in high temperature experiments," *Review of Scientific Instruments*, vol. 86, Article ID 035111, 2015.

[12] Y. Song, Y. Jiang, S. Ma, X. Yang, and T. Zhao, "Evolution of deformation fields and energy in whole process of rock failure," *Rock and Soil Mechanics*, vol. 33, no. 5, pp. 1352–1356+1365, 2012.

[13] Y. Pan and X. Yang, "A study on the deformation localization of rocks by white light digital speckle correlation method," *Journal of Experimental mechanics*, vol. 16, no. 2, pp. 220–225, 2001.

[14] G. Manthei and K. Plenkers, "Review on in situ acoustic emission monitoring in the context of structural health monitoring in mines," *Applied Sciences*, vol. 8, no. 9, Article ID 1595, 2018.

[15] X. Liu, H. Zhang, X. Wang et al., "Acoustic emission characteristics of graded loading intact and holey rock samples during the damage and failure process," *Applied Sciences*, vol. 9, no. 8, Article ID 1595, 2019.

[16] D. Shirole, A. Hedayat, and G. Walton, "Damage monitoring in rock specimens with pre-existing flaws by non-linear ultrasonic waves and digital image correlation," *International Journal of Rock Mechanics and Mining Sciences*, vol. 142, Article ID 104758, 2021.

[17] B. Yuan, W. Chen, Z. Li et al., "Sustainability of the polymer SH reinforced recycled granite residual soil: properties, physicochemical mechanism, and applications," *Journal of Soils and Sediments*, vol. 23, no. 1, pp. 246–262, 2023.

[18] B. Yuan, W. Chen, J. Zhao et al., "Addition of alkaline solutions and fibers for the reinforcement of kaolinite-containing granite residual soil," *Applied Clay Science*, vol. 228, Article ID 106644, 2022.

[19] Y. Zhao, L. Liu, Y. Pan, B. Jiao, and C. Zhang, "Experiment study on microseismic, charge induction, self-potential and acoustic emission during fracture process of rocks," *Chinese Journal of Rock Mechanics and Engineering*, vol. 36, no. 1, pp. 107–123, 2017.

[20] S. Liu, L. Wu, C. Wang, D. Ge, and Y. Wu, "Remote sensing-rock mechanics (VIII)–tir omens of rock fracturing," *Chinese Journal of Rock Mechanics and Engineering*, vol. 23, no. 10, pp. 1621–1627, 2004.

[21] S. Barone and E. A. Patterson, "The development of simultaneous thermo- and photo-elasticity for principal stress analyses," *Strain*, vol. 35, no. 2, pp. 57–65, 1999.

[22] Y. Zhang and S. Liu, "Thermal radiation temperature field variation of hole rock in loading process," *Rock and Soil Mechanics*, vol. 32, no. 4, pp. 1013–1017+1024, 2011.

[23] Y. Zhao and Y. Jiang, "Acoustic emission and thermal infrared precursors associated with bump-prone coal failure," *International Journal of Coal Geology*, vol. 83, no. 1, pp. 11–20, 2010.

[24] L. Wu, "Remote sensing rock mechanics and its recent achievements and future development," *Chinese Journal of Rock Mechanics and Engineering*, vol. 20, no. 2, pp. 139–146, 2001.

[25] L.-H. Chen, W.-C. Chen, Y.-C. Chen, L. Benyamin, and A.-J. Li, "Investigation of hydraulic fracture propagation using a post-peak control system coupled with acoustic emission," *Rock Mechanics and Rock Engineering*, vol. 48, no. 3, pp. 1233–1248, 2015.

[26] J.-P. Liu, R. Wang, G. Lei, Y.-T. Si, S.-D. Xu, and Y.-H. Li, "Studies of stress and displacement distribution and the evolution law during rock failure process based on acoustic emission and microseismic monitoring," *International Journal of Rock Mechanics and Mining Sciences*, vol. 132, Article ID 104384, 2020.

[27] J. Geng, Q. Sun, Y. Zhang, L. Cao, and W. Zhang, "Studying the dynamic damage failure of concrete based on acoustic emission," *Construction and Building Materials*, vol. 149, pp. 9–16, 2017.

[28] Y. Zhao, T. Yang, T. Xu, P. Zhang, and W. Shi, "Mechanical and energy release characteristics of different water-bearing sandstones under uniaxial compression," *International Journal of Damage Mechanics*, vol. 27, no. 5, pp. 640–656, 2018.

[29] J. Yang, Z.-L. Mu, and S.-Q. Yang, "Experimental study of acoustic emission multi-parameter information characterizing rock crack development," *Engineering Fracture Mechanics*, vol. 232, Article ID 107045, 2020.

[30] B. Gutenberg and C. F. Richter, "Frequency of earthquakes in California," *Bulletin of the Seismological Society of America*, vol. 34, no. 4, pp. 185–188, 1944.

[31] D. A. Lockner, J. D. Byerlee, V. Kuksenko, A. Ponomarev, and A. Sidorin, "Quasi-static fault growth and shear fracture energy in granite," *Nature*, vol. 350, pp. 39–42, 1991.

[32] M. V. M. S. Rao and K. J. P. Lakshmi, "Analysis of b-value and improved b-value of acoustic emissions accompanying rock fracture," *Current Science*, vol. 89, pp. 1577–1582, 2005.

[33] J.-S. Kim, K.-S. Lee, W.-J. Cho, H.-J. Choi, and G.-C. Cho, "A comparative evaluation of stress–strain and acoustic emission methods for quantitative damage assessments of brittle rock," *Rock Mechanics and Rock Engineering*, vol. 48, no. 2, pp. 495–508, 2015.

[34] B. Pan and K. Li, "A fast digital image correlation method for deformation measurement," *Optics and Lasers in Engineering*, vol. 49, no. 7, pp. 841–847, 2011.

[35] J. Blaber, B. Adair, and A. Antoniou, "Ncorr: open-Source 2D digital image correlation matlab software," *Experimental Mechanics*, vol. 55, no. 6, pp. 1105–1122, 2015.

[36] R. Harial and M. Ramji, "Adaptation of open source 2D DIC software Ncorr for solid mechanics applications," in *9th International Symposium on Advanced Science and Technology in Experimental Mechanics*, New Delhi, India, 2014.